

Far-Field Patterns of Plasmon Waveguide Interband Cascade Lasers

Zuwei Yin, Yuchao Jiang, Zhaobing Tian, Rui Q. Yang, *Senior Member, IEEE*,
Tetsuya D. Mishima, Michael B. Santos, and Matthew B. Johnson

Abstract—The far-field patterns of InAs-based plasmon-waveguide interband cascade lasers are experimentally and theoretically investigated. It is shown that different ridge waveguide structures and metal contact configurations lead to distinctive far-field patterns. With the commonly adopted center metal contact on the top of the ridge waveguide, an undesirable double-lobe far-field pattern along the lateral direction is exhibited, while with two metal contacts near the edges of the ridge or a broad-area metal contact on the mesa structure, the more desirable single lobe far-field pattern is observed. These characteristic far-field patterns and their implications are discussed with the aid of a theoretical model which is in good agreement with our experimental results.

Index Terms—Far-field, interband cascade laser, plasmon waveguide.

I. INTRODUCTION

COMPACT semiconductor mid-infrared (IR) laser sources are required for many applications, such as environmental monitoring, medical diagnostics, free space communication, and infrared countermeasures [1], [2]. Among IR laser sources, in the last decade, quantum cascade (QC) lasers [3] based on intersubband transitions in the well-established InP-based material system, have been widely investigated and have rapidly developed with remarkable high performance [4]–[7]. In contrast, interband cascade (IC) lasers [8] based on the InAs/GaSb type-II quantum well (QW) system, have not been explored extensively, although they possess certain advantages, most notably ease of establishing population inversion and low threshold current density [9], [10]. This is, in part, due to

the limited availability of GaSb-based growth facilities, consequently limiting the knowledge of optimal growth conditions and the development of device fabrication techniques. Two recent significant advancements are thermoelectrically-cooled single-mode distributed feedback (DFB) continuous wave (cw) IC lasers [11] and the demonstration of cw IC lasers above room temperature (up to 345 K) [12], [13]. Another recent advancement in IC lasers is the extension of their wavelengths to 7.5 μm , based on plasmon-waveguides on InAs substrates [14] instead of the GaSb substrates used earlier [10]–[13]. Nevertheless, many aspects of IC lasers are still to be investigated. For example, far-field patterns of IC lasers, which are important for integration with optical systems sensitive to beam divergence, have not been reported in a systematic manner in the literature. In this paper, we present a detailed study of the far-field patterns of plasmon waveguide IC lasers with different ridge dimensions and metal contact configurations. Distinctive far-field patterns, corresponding to the fundamental and the first excited optical modes, are observed with different metal contact arrangements. Theoretical calculations are used to model the experimental results and are found to provide good agreement. The implications of the experimental results and these calculations are discussed in connection with specific plasmon waveguide structures and the losses from the metal contact layers.

II. DEVICE CONFIGURATIONS AND EXPERIMENTAL SETUP

The mid-IR lasers investigated in this paper are InAs-based plasmon waveguide IC lasers with emission wavelength λ of about 5.6 μm (there were small variations ($<2\%$) on λ from device to device) at 80 K. The waveguide core structure consists of a 10-stage 0.5- μm -thick active region, and bottom and top n -type InAs separate confinement layers with thickness of 1.65 and 2.15 μm , respectively, which is sandwiched between a 1.5- μm -thick n^+ -type InAs bottom cladding and 35-nm-thick n^+ -type InAs top contact layers. Further details can be found in [15], [16]. The use of fewer stages and the absence of a thick top plasmon InAs cladding layer simplified the MBE growth. Pieces of the wafer were processed into ridge-waveguide laser devices with different top Ti/Au contact configurations on the ridges with various dimensions. As illustrated in Fig. 1 and listed in Table I, devices A to C are narrow-ridge devices, with ridge width of 15, 20, and 40 μm , respectively. A 200-nm-thick SiO_2 layer is deposited for electrical insulation from the wire bonding

Manuscript received May 9, 2011; revised August 10, 2011; accepted September 11, 2011. Date of current version October 4, 2011. This work was supported in part by the National Science Foundation under Grant ECCS-1002202, Center for Semiconductor Physics in Nanostructures, and the Oklahoma/Arkansas Materials Research Science and Engineering Center under Grant DMR-050550.

Z. Yin is with the School of Electrical and Computer Engineering, University of Oklahoma, Norman, OK 73019 USA. He is also with the Nanjing National Laboratory of Microstructures and School of Engineering and Applied Sciences, Nanjing University, Nanjing 210093, China (e-mail: yinzuwei@gmail.com).

Y. Jiang, Z. Tian, and R. Q. Yang are with the School of Electrical and Computer Engineering, University of Oklahoma, Norman, OK 73019 USA (e-mail: yuchao.jiang@ou.edu; zbtian@ou.edu; rui.q.yang@ou.edu).

T. D. Mishima, M. B. Santos, and M. B. Johnson are with the Homer L. Dodge Department of Physics and Astronomy, University of Oklahoma, Norman, OK 73019 USA (e-mail: mishima@ou.edu; santos@nhn.ou.edu; Matthew.B.Johnson-2@ou.edu).

Color versions of one or more of the figures in this paper are available online at <http://ieeexplore.ieee.org>.

Digital Object Identifier 10.1109/JQE.2011.2168812

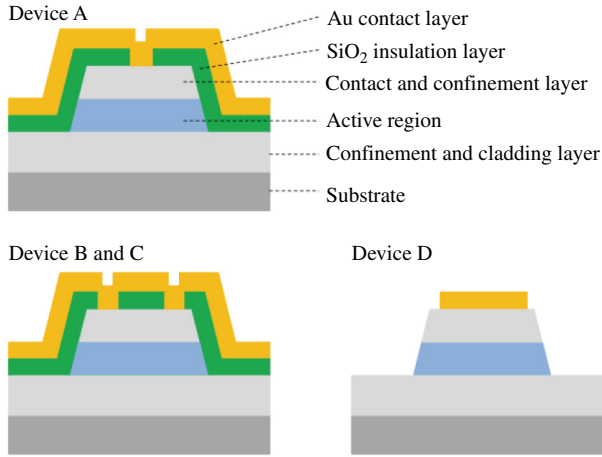


Fig. 1. Four IC laser device structures. Device A has a 15- μm -wide ridge with one metal contact trench in the center, devices B and C have two metal contact trenches near the edges (ridge width 20 and 40 μm , trench spacing 8 and 28 μm), device D is a 150- μm -wide laser with a 100- μm -wide Ti/Au metal stripe on the top of the mesa.

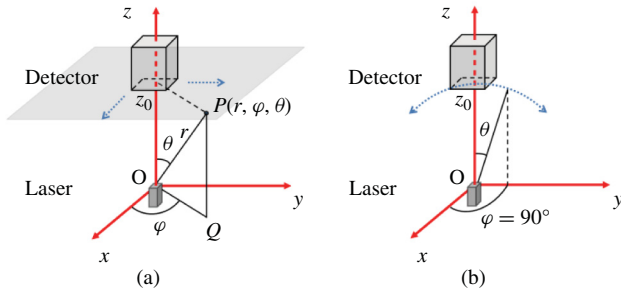


Fig. 2. Schematic drawing of the experimental setup for the far-field measurement. (a) Laser (or the detector) is moved along the x - y plane to map the 2-D light intensity profile. (b) Detector is rotated around the laser when φ is fixed at 90° .

pad and a Ti/Au ($\sim 30/170$ nm) layer is placed on the top of each device for contacts and the wire bonding pad. Device A has only one 2- μm -wide contact window on the top of the ridge stripe, which is the commonly adopted configuration for Fabry-Perot cavity diode lasers. Devices B and C have two contact windows near the two edges of the ridge, as shown in Fig. 1, with spacing of 8 and 28 μm , respectively. This double-contact window configuration was used in the past for DFB IC lasers to minimize losses from the top metal contact [11]. Device D is a broad-area laser, with a mesa width of 150 μm and a 100 μm -wide Ti/Au contact on the top of the center part of the mesa. The cavity lengths of the devices are around 1.8 mm.

The initial experimental setup for the far-field measurement is shown in Fig. 2(a). The laser devices were operated at 80 K inside a liquid nitrogen (LN_2) cooled cryostat that was set on a two-dimensional (2D) translational stage. The devices were driven by a pulsed current source, with a pulse width of 1 ms at repetition rate of 500 Hz. The far-field profile was collected by a LN_2 cooled mercury cadmium telluride (MCT) detector (active area size: 1 mm \times 1 mm). The MCT detector was placed on a three-dimensional (3D) translational stage

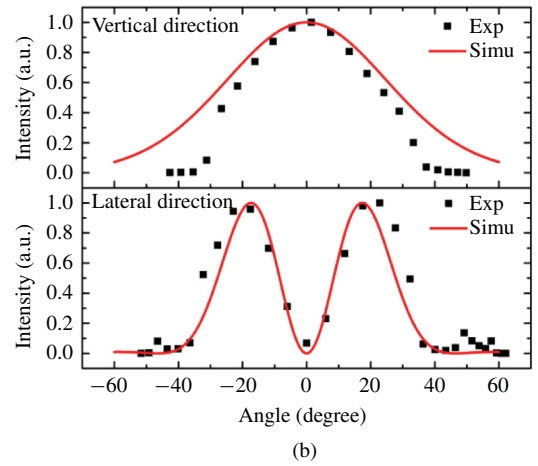
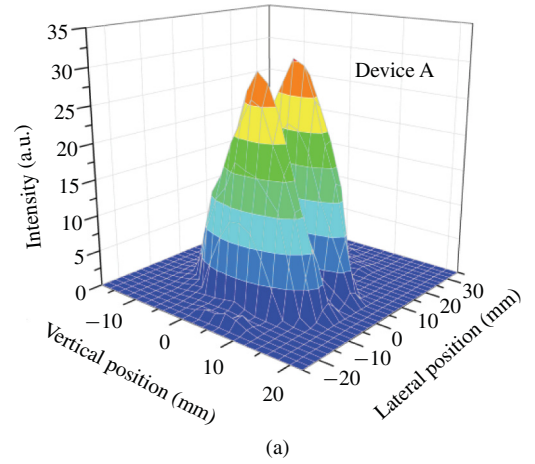


Fig. 3. (a) Measured far-field profile of device A under 18.0 mA. (b) Experimental (filled dots) and simulated (solid lines) far-field intensity of device A under a pulse current of 18.0 mA. The top panel is data along the vertical direction and the bottom panel is for the lateral direction.

19 mm away from the laser facet. A lock-in amplifier triggered by the pulsed current source was used to measure the signal from the MCT detector. Under high-injection conditions, an IR neutral density filter was placed in front of the MCT detector to prevent the detector from saturating.

The far-field pattern of a laser was obtained by moving either the detector or the laser in the x - y plane. As illustrated in Fig. 2(a), by assuming the laser was at the origin, the detector was moved on the $z = z_0$ plane so that its coordinates are (x, y, z_0) . Then, the far-field was converted to angle-dependent profiles at fixed φ for lateral and vertical directions. When the detector was moved along the x axis (or y axis), the angle φ remained at 0 (or 90°). Therefore, the measured intensity $P(x, y)$ can be converted to $P'(\theta)$ by the following equation:

$$P'(\theta) = \frac{P(x, y) \cdot r^2}{z_0^2 \cos \theta}$$

where $r = \sqrt{x^2 + y^2 + z_0^2}$, $P'(\theta)$ is the converted intensity, and θ is the far-field angle along the lateral or vertical direction. In this conversion, we assumed that the detector response was independent of the incident angle and the light

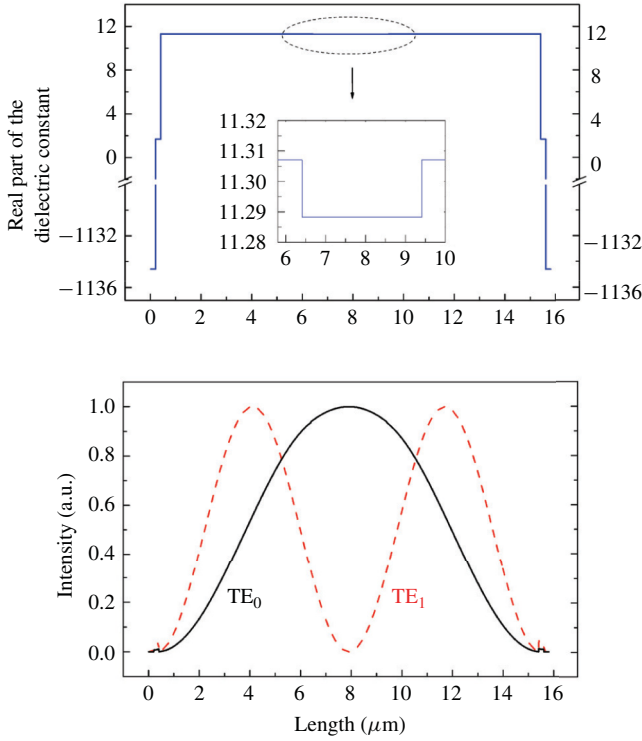


Fig. 4. Top panel is the profile of the real part of the dielectric constant along the lateral direction and the bottom panel is the calculated near-field intensity of the fundamental (solid) and the first-order (dashed) modes along the lateral direction. The inset is the dielectric constant profile at the center of the ridge.

intensity was uniform across the active area of the detector, which should be a good approximation when the detector area is small and z_0 is large.

In the vertical direction, the laser beam is very divergent (about $\pm 60^\circ$) and the far-field measurement made by moving the detector (or laser) in the x-y plane, as described above, was not accurate at an angle close to or larger than the field of view ($\pm 33^\circ$) of the detector. To better measure the far-field along the vertical direction, the detector was later placed on the arm of a rotation stage centered at the laser position. In this configuration, the detector is a fixed distance to the laser as it rotates around the laser as shown in Fig. 2(b) and always faces the laser at any angle without being limited by its finite field of view.

III. EXPERIMENTAL RESULTS AND DISCUSSION

The far-field pattern of device A under a current injection at the level of about 1.1 times the threshold current (I_{th}) is shown in Fig. 3(a). As one can see, the far-field pattern along the vertical axis (the growth direction) exhibits a single-lobe profile, while on the lateral direction, double peaks are observed, which indicates the dominance of the first-order lateral mode over the fundamental (zero-order) mode. The far-field profiles with respect to angles along the growth direction and lateral direction are shown in Fig. 3(b). The full width at half maximum (FWHM) is 49.9° along the growth direction, which is not accurate due to the limited field of view for the

detector. We will comment on this later in the paper. The FWHM of the far-field is 23.1° for each lobe along the lateral direction. This observation suggests that the commonly used center metal contact configuration might introduce more loss to the fundamental mode than the first-order mode, leading to a more divergent beam with two peaks in the far-field pattern, which is undesirable.

To model the experimental profiles, an effective index method was used to calculate the waveguide losses and mode profiles in both lateral and vertical directions in the ridge waveguide [17]–[19]. Fig. 4 shows the simulated near-field intensity of the fundamental and first-order modes, and the real part of the effective dielectric constant $\text{Re}(\epsilon)$ along the lateral direction of device A. The real parts of dielectric constants for seven equivalent layers (metal, oxide, left region, center, right region, oxide, metal) along the lateral direction of device A are -1134.58 , 1.69 , 11.31 , 11.29 , 11.31 , 1.69 , and -1134.58 , respectively. The corresponding thicknesses are 0.2 , 0.2 , 6.0 , 3.0 , 6.0 , 0.2 and $0.2 \mu\text{m}$, respectively. Owing to the stronger coupling of the fundamental mode with the center metal contact, the calculated free carrier absorption loss in the waveguide for the fundamental TE mode is 3.91 cm^{-1} , which is slightly higher than for the first-order lateral mode (3.65 cm^{-1}). In other words, the threshold gain required for lasing is lower for the first-order lateral mode than for the fundamental mode. Hence, the device lased first in the first-order mode with two peaks appearing in the far-field pattern. As shown in Fig. 3(b) (solid lines), the calculated far-field profile along the lateral direction, obtained by Fourier transform from the near-field, is in good agreement with our experimental result. The FWHM for each lobe in the simulation (19.4°) is slightly smaller, which may be due to the simplification of the theoretical calculation and possible experimental uncertainties. Also as shown in the top panel of Fig. 3(b), when the angle is larger than 30° , the calculated far-field intensity is higher than the measured value. This is because the detector is located inside a dewar about 10 mm away from the dewar window and thus has a limited field of view as mentioned earlier. Based on the dewar geometry and the detector size, we estimate that a reduced amount of laser light reaches the detector for incident angles larger than 33° and no unscattered light reaches the detector for angles larger than 38° . The detector may still receive some scattered laser light when the incident angle is larger than 38° , but the intensity is not accurate. Hence, the measured intensity is underestimated when the incident angle is larger than 33° . Nevertheless, the qualitative features of the far-field patterns are not affected (only their FWHMs are slightly narrower than the actual values when the beam is very divergent), which is verified by later measurements on other devices using a rotation stage.

Fig. 5 is the lateral far-field profiles of device A under various injection conditions (1.1 to 10 times I_{th}) which show that the valley floor between two lobes rises with the increasing current. This is because as the injection current increases, the fundamental TE mode also reaches the threshold gain (its waveguide loss is only 0.26 cm^{-1} higher than the first-order mode), leading to modal mixing with the first-order mode.

TABLE I
PARAMETERS OF FOUR DIFFERENT DEVICES

Device number	Ridge width (μm)	Cavity length (mm)	Metal contact pattern	Pulse current (mA)	Experiment		Simulation	
					Lateral FWHM ($^\circ$)	Vertical FWHM ($^\circ$)	Lateral FWHM ($^\circ$)	Vertical FWHM ($^\circ$)
A	15	1.8	single	18.0	23.1 ± 1.2 for each lobe	*	19.4 for each lobe	59.0
B	20	1.8	double	21.5	17.3 ± 0.9	54.7	18.7	59.0
C	40	1.8	double	61.0	9.2 ± 0.5	54.4	9.18	59.0
D	150	1.86	whole	138	10.1 ± 0.6	55.2	*	60.2

* See descriptions in Section III.

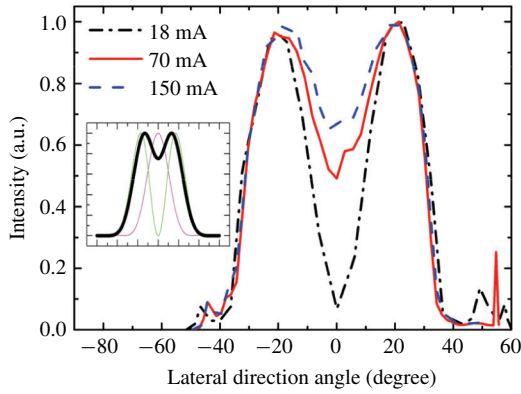


Fig. 5. Far-field profiles of device A under different pulse currents along the lateral direction. The inset illustrates that the far-field intensity (dark black line) is a combination of the fundamental mode (purple) and the first mode (light green) (composed of equal portions of the fundamental mode and the first-order mode).

The inset to Fig. 5 gives an illustrative far-field profile that has equal contributions from the fundamental and the first-order modes. Again, the sharp drops near 33° of the measured intensity in Fig. 5 were due to the limited field of view of the detector.

The measured far-field profiles of devices A through D along both the vertical and the lateral directions are plotted in Fig. 6. All the devices were driven at current levels of around 1.1 times I_{th} at 80 K. The FWHM of each profile is listed in Table I. The far-field distributions along the vertical axis all have a FWHM about 55° , and were obtained with the rotation stage (except for device A that was damaged before the rotation stage was set-up). This value is in a good agreement with the calculated value ($\sim 59^\circ$) for the fundamental mode in the vertical direction. In the simulation of the far-field profile along the vertical axis, a one-dimensional model was used, in which only the variation of the dielectric constant along the vertical direction was considered, while the Au and SiO_2 layers were treated as two flat layers without considering the lateral variation (*e.g.* small metal contact window in the SiO_2 layer). This simplification gave the same far-field FWHMs along the vertical axis for all of the narrow-ridge lasers, while the FWHM of the broad-area device was slightly larger due to the absence of a SiO_2 layer between the top metal contact and the semiconductor mesa. The vertical far-field patterns of devices were also examined under different

currents. Essentially, no changes of their vertical far-field patterns were observed for these devices.

Along the lateral direction the far-field profiles of devices B and C exhibit a single-lobe profile (unlike device A), which are in agreement with our simulation results. The two edge metal contacts on the ridge lead to a single-lobe far-field profile along the lateral direction, corresponding to the fundamental mode in the lateral direction. In addition, the larger spacing between the two metal contacts made a less divergent far-field pattern as indicated by the smaller FWHM ($\sim 9.2^\circ$) for the $40\text{-}\mu\text{m}$ -wide ridge device C compared to the FWHM value ($\sim 17.3^\circ$) for the $20\text{-}\mu\text{m}$ -wide ridge device B, in excellent agreement with the simulation results (Fig. 6(b) and Table I) based on the fundamental lateral mode. However, for the **broad-area** ($150\text{-}\mu\text{m}$ -wide mesa-stripe) device D, the observed single-peak profile along the lateral direction with a FWHM of 10.1° could **be a collective reflection of several modes with higher-order divergent components**. Many lateral modes in the broad-area device have nearly the same threshold gain and could lase at the same current. Hence, the far-field profile along the lateral direction could not be obtained based on a simple single-mode near-field calculation. A superposition of multiple modes ($0\sim 4$ th order modes $\text{TE}_{00}:\text{TE}_{01}:\text{TE}_{02}:\text{TE}_{03}:\text{TE}_{04} = 4:4:3:3:2$) was used to achieve a reasonable agreement with the experimental curve as shown in Fig. 6(b).

On the whole, there are small differences in the FWHM values between the experimental and simulated profiles, particularly for the far-field along the vertical direction. Below we summarize the errors in order of significance, starting with the most significant. As described above for the measurement using a translation stage moving in the x-y plane, the most significant error is associated with the detector's finite field of view, which results in the reduction of the detected laser intensity at an incident angle larger than 33° . A second error is associated with the inaccuracy of z_0 in our set-up. This is due to the inaccuracy of the exact position of the MCT detector within its dewar (the position is specified to the nearest mm). In our setup we use a distance between the laser and detector of 19 mm, in order to measure the entire far-field pattern. The 5% inaccuracy in z_0 results in a 10% maximum error in our measured FWHMs of the far-field patterns. The error due to the detector's finite field of view was circumvented by using a rotation stage. Nevertheless, there are some difficulties using the rotation stage to measure the far-field patterns. For

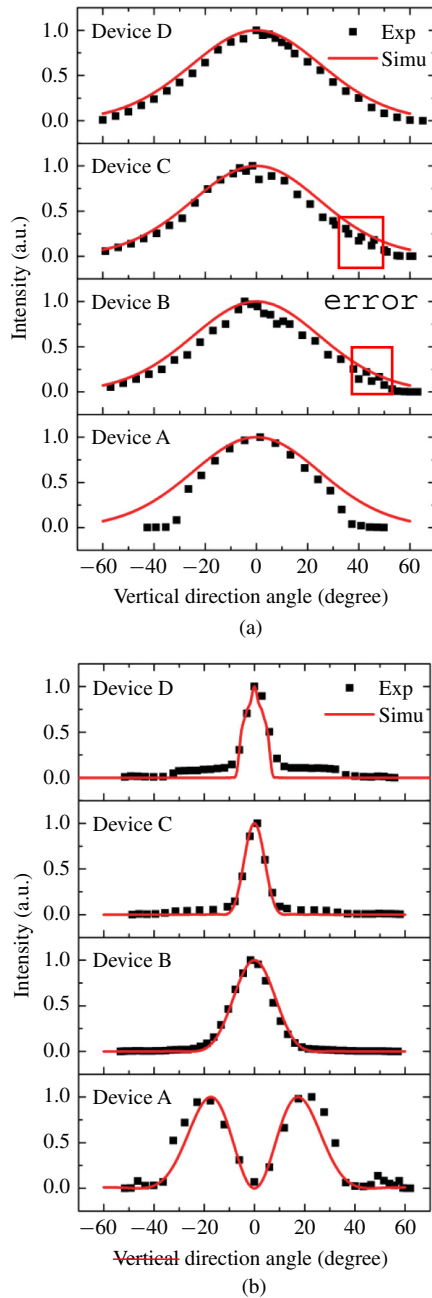


Fig. 6. Far-field intensity for four devices as functions of angle along (a) vertical direction and (b) lateral direction.

example, the rotation axis must be accurately positioned at the center of the laser facet, and the rotation plane of the detector should be parallel to the laser facet. Deviations from these requirements will result in some error. Another factor affecting the intensity of the far-field patterns is the instability of the laser. This was most pronounced when there was mixing of different laser modes under high-current injection. The largest intensity variation was about 2%, which could lead to small errors ($<1.4\%$) in calculating the FWHM. Finally, temperature fluctuations during the times required for intensity scans could also cause some intensity variations. However, the observed maximum temperature fluctuation of about 0.02 K at 80 K,

should not lead to substantial error. In summary, considering all possible factors that may contribute to the difference of the observed and calculated FWHMs along the vertical axis ($\sim 15\%$ with the translation stage method, $\sim 5\%$ with the rotation stage), the measured results are in good agreement with the calculations.

IV. CONCLUSION

Far-field patterns of plasmon waveguide IC lasers have been investigated along the vertical and the lateral directions. It has been observed that the commonly adopted center metal contact configuration leads to an **undesirable double-lobe far-field pattern associated with the first-order lateral mode** in plasmon waveguide IC lasers. With two metal contacts placed near the edges of the ridge, a more desirable, less divergent single-lobe beam was exhibited in the far-field. The experimentally observed far-field profiles agree well with simulated results. This study suggests that appropriate metal contact configurations need to be considered in the design of plasmon IC lasers, especially when a thick top semiconductor cladding layer is absent.

ACKNOWLEDGMENT

The authors would like to thank R. T. Hinkey for helpful discussions on waveguide calculations. Z. Yin is grateful to X. Chen of Nanjing University, Nanjing, China, for his beneficial guidance in the research.

REFERENCES

- [1] R. D. Hudson, *Infrared System Engineering*. New York: Wiley, 1969.
- [2] P. Werle, "A review of recent advances in semiconductor laser based gas monitors," *Spectrochim. Acta Part A*, vol. 54, no. 2, pp. 197–236, Feb. 1998.
- [3] J. Faist, F. Capasso, D. L. Sivco, C. Sirtori, A. L. Hutchinson, and A. Y. Cho, "Quantum cascade laser," *Science*, vol. 264, no. 5158, pp. 553–556, Apr. 1994.
- [4] M. Beck, D. Hofstetter, T. Aellen, J. Faist, U. Oesterle, M. Illegems, E. Gini, and H. Melchior, "Continuous wave operation of a mid-infrared semiconductor laser at room temperature," *Science*, vol. 295, no. 5553, pp. 301–305, Jan. 2002.
- [5] A. Lyakh, C. Pflügl, L. Diehl, Q. J. Wang, F. Capasso, X. J. Wang, J. Y. Fan, T. Tanbun-Ek, R. Maulini, A. Tsekoun, R. Go, and C. K. N. Patel, "1.6 W high wall plug efficiency, continuous-wave room temperature quantum cascade laser emitting at 4.6 μm ," *Appl. Phys. Lett.*, vol. 92, no. 11, pp. 111110-1–111110-3, Mar. 2008.
- [6] M. Razeghi, "High-performance InP-based mid-IR quantum cascade lasers," *IEEE J. Sel. Topics Quantum Electron.*, vol. 15, no. 3, pp. 941–951, May–Jun. 2009.
- [7] R. F. Curl, F. Capasso, C. Gmachl, A. A. Kosterev, B. McManus, R. Lewicki, M. Pusharsky, G. Wysocki, and F. K. Tittel, "Quantum cascade lasers in chemical physics," *Chem. Phys. Lett.*, vol. 487, nos. 1–3, pp. 1–18, Feb. 2010.
- [8] R. Q. Yang, "Infrared laser based on intersubband transitions in quantum wells," *Superlatt. Microstruct.*, vol. 17, no. 1, pp. 77–83, Jan. 1995.
- [9] J. R. Meyer, I. Vurgaftman, R. Q. Yang, and L. R. Ram-Mohan, "Type-II and type-I interband cascade lasers," *Electron. Lett.*, vol. 32, no. 1, pp. 45–46, Jan. 1996.
- [10] R. Q. Yang, "Novel concepts and structures for infrared lasers," in *Long Wavelength Infrared Emitters Based on Quantum Wells and Superlattices*, M. Helm, Ed. Singapore: Gordon & Breach, 2000, ch. 2, pp. 13–64.
- [11] R. Q. Yang, C. J. Hill, K. Mansour, Y. Qiu, A. Soibel, R. E. Muller, and P. M. Echternach, "Distributed feedback mid-IR interband cascade lasers at thermoelectric cooler temperatures," *IEEE J. Sel. Topics Quantum Electron.*, vol. 13, no. 5, pp. 1074–1078, Sep.–Oct. 2007.

- [12] M. Kim, C. L. Canedy, W. W. Bewley, C. S. Kim, J. R. Lindle, J. Abell, I. Vurgaftman, and J. R. Meyer, "Interband cascade laser emitting at $\lambda = 3.75 \mu\text{m}$ in continuous wave above room temperature," *Appl. Phys. Lett.*, vol. 92, no. 19, pp. 191110-1–191110-3, May 2008.
- [13] W. W. Bewley, C. L. Canedy, C. S. Kim, M. Kim, J. R. Lindle, J. Abell, I. Vurgaftman, and J. R. Meyer, "Ridge-width dependence of midinfrared interband cascade laser characteristics," *Opt. Eng.*, vol. 49, no. 11, pp. 111116-1–111116-5, Nov. 2010.
- [14] Z. Tian, R. Q. Yang, T. D. Mishima, M. B. Santos, and M. B. Johnson, "Plasmon-waveguide interband cascade lasers near $7.5 \mu\text{m}$," *IEEE Photon. Technol. Lett.*, vol. 21, no. 21, pp. 1588–1590, Nov. 2009.
- [15] Z. Tian, R. Q. Yang, T. D. Mishima, M. B. Santos, R. T. Hinkey, M. E. Curtis, and M. B. Johnson, "InAs-based interband cascade lasers near $6 \mu\text{m}$," *Electron. Lett.*, vol. 45, no. 1, pp. 48–49, Jan. 2009.
- [16] Z. Tian, C. Chen, R. Q. Yang, T. D. Mishima, M. B. Santos, J. C. Keay, M. B. Johnson, and J. F. Klem, "InAs-based plasmon-waveguide interband cascade lasers," *Proc. SPIE*, vol. 7616, p. 76161B, Jan. 2010.
- [17] G. B. Hocker and W. K. Burns, "Mode dispersion in diffused channel waveguides by the effective index method," *Appl. Opt.*, vol. 16, no. 1, pp. 113–118, Jan. 1977.
- [18] K. S. Chiang, "Dual effective-index method for the analysis of rectangular dielectric waveguides," *Appl. Opt.*, vol. 25, no. 13, pp. 2169–2174, Jul. 1986.
- [19] J. Buus, "The effective index method and its application to semiconductor lasers," *IEEE J. Quantum Electron.*, vol. 18, no. 7, pp. 1083–1089, Jul. 1982.

Zuowei Yin was born in Yancheng, China, in 1985. He received the B.S. degree from Nanjing University, Nanjing, China, in 2007. He is currently pursuing the Ph.D. degree with the National Laboratory of Microstructures and School of Engineering and Applied Sciences, Nanjing University. He is currently supported by China Council Scholarship as a Visiting Graduate Student with the University of Oklahoma, Norman.

His current research interests include fiber communication and semiconductor devices such as interband cascade lasers.

Yuchao Jiang received the B.S. degree from the Beijing University of Posts and Telecommunications, Beijing, China, and the M.S. degree from the Institute of Semiconductors, Chinese Academy of Science, Beijing, in 2007 and 2011, respectively. He is currently pursuing the Ph.D. degree with the School of Electrical and Computer Engineering, University of Oklahoma, Norman.

His current research interests include mid-infrared lasers such as quantum and interband cascade lasers.

Zhaobing Tian received the B.E. degree in electrical engineering from Xi'an Jiaotong University, Xi'an, China, and the Ph.D. degree in solid-state and micro-electronics from the Shanghai Institute of Microsystem and Information Technology, Chinese Academy of Sciences, Shanghai, China, in 2003 and 2008, respectively.

He is currently with the School of Electrical and Computer Engineering, University of Oklahoma, Norman. His current research interests include physics and development of infrared optoelectronic devices, including lasers, detectors, and photovoltaic devices.

Rui Q. Yang (M'95–SM'02) received the Ph.D. degree in physics from Nanjing University, Nanjing, China, in 1987.

He is a Professor with the School of Electrical and Computer Engineering, University of Oklahoma (OU), Norman. Prior to joining OU in 2007, he was a Principal Member of Engineering Staff and a Task Manager with the Jet Propulsion Laboratory (JPL), Pasadena, CA. He has authored or co-authored more than 100 refereed journal articles and one book chapter. His current research interests include condensed matter physics to semiconductor quantum devices such as mid-infrared lasers, detectors, and photovoltaic devices.

Dr. Yang received the Edward Stone Award in 2007 from JPL for Outstanding Research Publication and the successful accelerated infusion of cutting-edge interband cascade semiconductor laser technology into flight mission readiness.

Tetsuya D. Mishima received the Ph.D. degree from Waseda University, Tokyo, Japan, in 1999.

He has been a Research Scientist with the University of Oklahoma, Norman, since 2001. He previously held a post-doctoral position at Pennsylvania State University, University Park, from 1999 to 2001. He is the co-author of about 70 scientific publications. His current research interests include structural defect reduction in semiconductor structures grown by molecular beam epitaxy, development of transmission electron microscopy techniques for structural defect analysis, and theoretical analysis on carrier transport in quantum well structures.

Michael B. Santos received the B.S. degree in electrical engineering and materials science from Cornell University, Ithaca, NY, and the Ph.D. degree in electrical engineering from Princeton University, Princeton, NJ, in 1986 and 1992, respectively.

He was a Post-Doctoral Researcher with AT&T Bell Laboratories, Holmdel, NJ, before joining the University of Oklahoma, Norman, in 1993. He is currently a Professor of physics with the University of Oklahoma. He has co-authored 190 papers on experimental semiconductor research.

Matthew B. Johnson received the B.S. degree in physics from the University of Waterloo, Waterloo, ON, Canada, and the Ph.D. degree in applied physics from the California Institute of Technology, Pasadena, in 1979 and 1989, respectively.

He has been a Physics Faculty Member with the University of Oklahoma, Norman, since 1995. He previously held post-doctoral positions at the IBM Research, Yorktown Heights, NY, and then the Swiss Federal Institute of Technology Zürich, Zürich, Switzerland. He has been serving as the Director of the Center for Semiconductor Physics in Nanostructures, National Science Foundation Materials Research Science and Engineering Center with members at the University of Oklahoma, and the University of Arkansas, Fayetteville, since 2000. He has co-authored over 100 scientific publications.